

# Understanding the Features of Crystal Structure, Electronic Structure and Electrical Conductivity of RuO<sub>2</sub>-SiO<sub>2</sub> Binary Oxides

Qifan Wang<sup>1</sup>, Yukun Wu<sup>1</sup>, Kongfa Chen<sup>1</sup>, Na Ai<sup>2</sup>, Xin Wang<sup>1,\*</sup>, Dian Tang<sup>1,\*</sup>

<sup>1</sup> College of Materials Science and Engineering, Fuzhou University, Fuzhou, Fujian 350108, China

<sup>2</sup> Testing Center, Fuzhou University, Fuzhou, Fujian 350108, China

\*E-mail: [xinxinwx@fzu.edu.cn](mailto:xinxinwx@fzu.edu.cn) (Xin Wang), [tangdian@fzu.edu.cn](mailto:tangdian@fzu.edu.cn) (Dian Tang)

Received: 5 February 2019 / Accepted: 25 March 2019 / Published: 31 May 2021

Density functional theory calculations combined with experiments were performed to investigate the stability, crystal structure, electronic structure and conductivity of RuO<sub>2</sub>-SiO<sub>2</sub> binary oxides. Our calculations indicate that Ru<sub>1-x</sub>Si<sub>x</sub>O<sub>2</sub> solid solutions are unstable, and both their total energies and lattice parameters deviate from Vegard's law, revealing a strong interaction between RuO<sub>2</sub> and SiO<sub>2</sub>. With an increase in  $x$  (doping concentration of SiO<sub>2</sub>), the conductivity of Ru<sub>1-x</sub>Si<sub>x</sub>O<sub>2</sub> underwent first-order exponential attenuation, but the compound remained metallic even when  $x$  was 0.875. Ru<sub>0.5</sub>Si<sub>0.5</sub>O<sub>2</sub>/Ti electrodes were prepared using the thermal decomposition method, and at different annealing temperatures, varying degrees of phase separation were observed in all the samples, proving the instability of the Ru<sub>1-x</sub>Si<sub>x</sub>O<sub>2</sub> solid solutions. The impedance test of the Ru<sub>0.5</sub>Si<sub>0.5</sub>O<sub>2</sub>/Ti samples showed that the total impedance of the samples and the degrees of phase separation conform to the first-order exponential relationship. The dual effects of Si doping attenuation and phase separation attenuation can explain the rapid decline in the conductivity of the RuO<sub>2</sub>-SiO<sub>2</sub> electrode material.

**Keywords:** First-principles; RuO<sub>2</sub>-SiO<sub>2</sub> binary oxide; crystal structure; phase separation; electronic structures; electrical conductivity

## 1. INTRODUCTION

Precious metal oxides are important active materials in the electrochemical industry owing to their superior electrocatalytic activity, high conductivity, and good corrosion resistance. RuO<sub>2</sub> is a common metal oxide and has often been used with non-precious metal oxides in binary oxide materials such as RuO<sub>2</sub>-SnO<sub>2</sub>[1], RuO<sub>2</sub>-TiO<sub>2</sub>[2], RuO<sub>2</sub>-ZrO<sub>2</sub>[3, 4], RuO<sub>2</sub>-CeO<sub>2</sub>[5, 6], RuO<sub>2</sub>-Ta<sub>2</sub>O<sub>5</sub>[7], and RuO<sub>2</sub>-MnO<sub>2</sub>[8]; this reduces the consumption of precious metals and may improve the electrode activity[9]. SiO<sub>2</sub> is an inert and insulating non-precious metal oxide, and it was considered a doping component later

than others; however, owing to abundant reserves and a low price, RuO<sub>2</sub>-SiO<sub>2</sub> can be utilized in electronic, electrochemical, and new energy applications, including evolution reactions[10, 11], electrocatalyst[12], photocatalyst[13], membrane materials[14] and fuel cells[15].

Since SiO<sub>2</sub> is an inert oxide that is significantly different from the active oxide RuO<sub>2</sub>, mixing them can lead to significant changes in structure and properties. In the field of structural research, the sol-gel method is generally used[13, 16-18]; an amorphous structure is obtained before annealing treatment, and rutile crystals are formed by annealing at a conventional temperature ( $\geq 400$  °C). The observed rutile phases are all Ru-related phases or pure RuO<sub>2</sub> phases, but researchers have not elucidated the transformation process of the composite structures; moreover, the characteristics of solid solutions have not been described quantitatively. In terms of performance, different compositions result in enormous changes in activity and conductivity, and research[17, 19] shows that a low concentration of Si is beneficial to improve activity, whereas a high concentration of Si leads to a sharp decrease in activity; an extraordinarily wide resistivity range can be achieved by adjusting the Si/Ru ratio. However, researchers have not discussed the changes in structure and performance in depth. To analyze these problems from the perspective of the mechanism, density functional theory (DFT) calculations were carried out in this study to analyze the energy and crystal structure characteristics of various compositions of Ru<sub>1-x</sub>Si<sub>x</sub>O<sub>2</sub> (solid solution) and then investigate the electronic structure and conductivity. Highly Si-doped solid solution samples were prepared using the thermal decomposition method, and Ru<sub>0.5</sub>Si<sub>0.5</sub>O<sub>2</sub> (composite) samples with varying degrees of phase separation were chosen to study the structure and conductivity. By combining the DFT calculations and experimental data, this report reveals the electronic structure and conductivity mechanism of RuO<sub>2</sub>-SiO<sub>2</sub> and discusses the intrinsic reasons for the interaction between RuO<sub>2</sub> and SiO<sub>2</sub> in the solid solution and composite.

## 2. METHODS SECTION

### 2.1 Computational Details

Our calculations were based on DFT as implemented in the Vienna ab initio simulation package (VASP)[20-22]. Projector augmented wave (PAW)[23] potentials were employed to describe ion-electron interactions, whereas the exchange-correlation interactions were treated using the Perdew-Burke-Ernzerhof (PBE)[24] generalized gradient approximation (GGA)[25]. The energy cutoff of the plane wave was 520 eV. Atomic relaxations were performed until convergence was achieved with a tolerance of 10<sup>-6</sup> eV in energy, 0.001 eV/Å in force, and 2×10<sup>-4</sup> nm in displacement. K-point sampling of 8×8×8 was used for structure relaxation and static calculations, and Ru: 4d<sup>7</sup>5s<sup>1</sup>, O: 2s<sup>2</sup>2p<sup>4</sup>, and Si: 3s<sup>2</sup>3p<sup>3</sup> were chosen as the valence-electron configurations. For the Si doping studies, each supercell contained 2×2×1 primitive cells of rutile RuO<sub>2</sub>.

The Murnaghan equation of state[26], Equation (1), was then applied to fit the calculated *E-V* curve to obtain *E*<sub>0</sub>, *V*<sub>0</sub>, and the equilibrium lattice parameters for Ru<sub>1-x</sub>Si<sub>x</sub>O<sub>2</sub> with various SiO<sub>2</sub> fractions.

$$E_{Murn}(V) = -E_0 + \frac{B_0 V}{B'_0} \left[ \frac{(V_0/V)^{B'_0}}{B'_0 - 1} + 1 \right] - \frac{B_0 V_0}{B'_0 - 1} \quad (1)$$

Both substitutional doping and interstitial doping were considered, and we found that the former had a lower total energy, which indicates a more stable structure; therefore, we substituted some Si for Ru in  $\text{Ru}_8\text{O}_{16}$  to achieve a series of supercells,  $\text{Ru}_8\text{O}_{16}$ ,  $\text{Ru}_7\text{SiO}_{16}$ ,  $\text{Ru}_6\text{Si}_2\text{O}_{16}$ ,  $\text{Ru}_5\text{Si}_3\text{O}_{16}$ ,  $\text{Ru}_4\text{Si}_4\text{O}_{16}$ ,  $\text{Ru}_3\text{Si}_5\text{O}_{16}$ ,  $\text{Ru}_2\text{Si}_6\text{O}_{16}$ ,  $\text{RuSi}_7\text{O}_{16}$ , and  $\text{Si}_8\text{O}_{16}$ , among which, the  $\text{Ru}_8\text{O}_{16}$  and  $\text{Ru}_4\text{Si}_4\text{O}_{16}$  supercells are shown in Fig. 1.

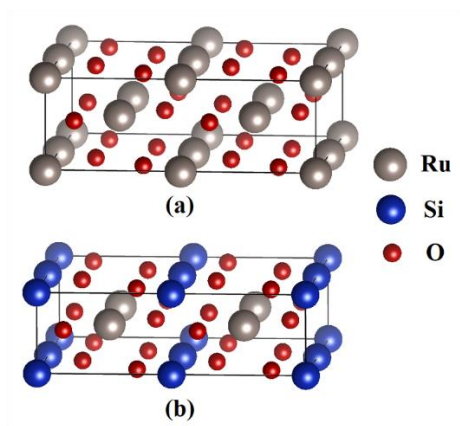


**Figure 1.** (a)  $\text{Ru}_8\text{O}_{16}$  rutile supercell and (b)  $\text{Ru}_4\text{Si}_4\text{O}_{16}$  rutile supercell.

## 2.2 Sample Preparation

A  $\text{Ru}_{0.5}\text{Si}_{0.5}\text{O}_2/\text{Ti}$  electrode was prepared via the thermal decomposition method, using industrial pure titanium TA2 as the substrate, and ruthenium trichloride (containing 36.9% Ru) and tetraethyl orthosilicate (97% purity) as the source materials. The pretreated titanium substrate was soaked in a 5% detergent heated-solution, and after washing with distilled water, it was etched in 10% oxalic acid for 1 h to obtain a titanium substrate having a rough surface. To achieve the doping of a high concentration of Si, the above raw materials were weighed according to an Si/Ru molar ratio of 1/1, and dissolved in absolute ethanol individually; appropriate additives were added, and the materials were dissolved uniformly using ultrasonic stirring. After allowing the mixture to stand for 24 h, a ruthenium silicon coating solution was obtained. This solution was coated on the pretreated titanium substrate, using a pipette, and dried under infrared light. The coated substrate was placed in a drying oven at 120 °C for 10 min, and air-cooled; the above operation was repeated 20 times. Then, annealing was performed at 240 °C, 260 °C, 280 °C, and 420 °C for 1 h each to prepare  $\text{Ru}_{0.5}\text{Si}_{0.5}\text{O}_2$  coated samples with a thickness of about 3  $\mu\text{m}$  and different degrees of phase separation.

## 2.3 Sample Test

Phase analyses of the oxide coatings were carried out using an X-ray diffractometer (XRD; Philips X'Pert MPD), with a copper  $\text{K}\alpha$  source ( $\lambda = 1.5406 \text{ \AA}$ ) and Ni filtration, at an accelerating voltage of 40 kV and a current of 40 mA. A scanning rate of 2°/min with a step length of 0.02° was used. XRD peak fitting was carried out using JADE software.

For high-resolution transmission electron microscopy (HRTEM), sample powder peeled off the titanium substrate was ultrasonically dispersed in an ethanol solution and loaded on a carbon-coated copper grid. The samples were examined under a field-emission HRTEM device (Tecnai G2 F20 S-TWIN, FEI, Inc.).

Electrochemical impedance spectroscopy (EIS) was performed in the frequency range of 0.01 Hz to 1 MHz. The impedance data were collected at a potential of 0.5 V with an amplitude of 5 mV. The experiments were carried out in 0.5 M H<sub>2</sub>SO<sub>4</sub> solutions at 25±1 °C, in a three-compartment all-glass cell (120 mL).

### 3. RESULTS AND DISCUSSION

#### 3.1 Structure and Stability of Rutile Ru<sub>1-x</sub>Si<sub>x</sub>O<sub>2</sub>

To analyze the stability of each rutile Ru<sub>1-x</sub>Si<sub>x</sub>O<sub>2</sub> supercell, we calculated the total energy ( $E_t$ ) of these supercells for different volumes ( $V$ ), and obtained the  $E$ - $V$  data. The Murnaghan equation of state was then applied to fit the  $E$ - $V$  curve, as shown in Fig. 2, and finally, the equilibrium total energy ( $E_0$ ) of each Ru<sub>1-x</sub>Si<sub>x</sub>O<sub>2</sub> supercell for various  $x$  values was found.

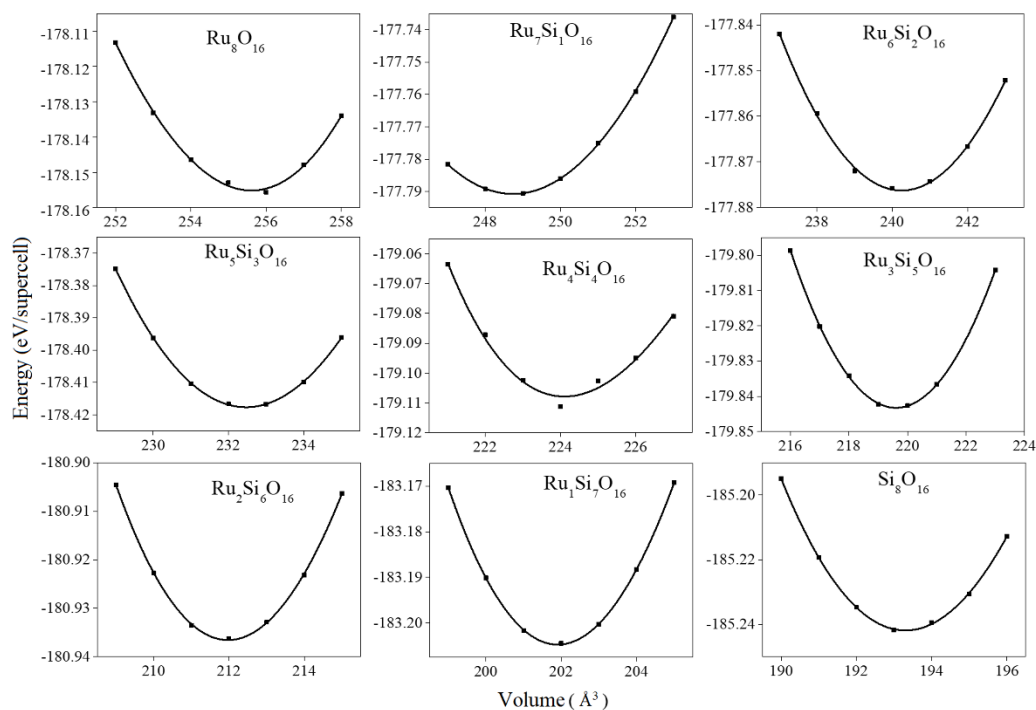


**Figure 2.** The calculated total energies of each Ru<sub>1-x</sub>Si<sub>x</sub>O<sub>2</sub> supercell as a function of  $V$ .

Fig. 3 shows the equilibrium total energy  $E_0$  of different composition Ru<sub>1-x</sub>Si<sub>x</sub>O<sub>2</sub> supercells as a function of the Si doping amount  $x$ . The equilibrium energy  $E_0$  of each composition of Ru<sub>1-x</sub>Si<sub>x</sub>O<sub>2</sub> is significantly higher than the average value given by Vegard's law[27] (shown by the dashed line). This

implies that the energy of  $\text{Ru}_{1-x}\text{Si}_x\text{O}_2$  is higher than the energy of the composite obtained by mixing  $\text{RuO}_2$  and  $\text{SiO}_2$ , which indicates that  $\text{Ru}_{1-x}\text{Si}_x\text{O}_2$  solid solutions are unstable, and they tend to decompose into  $(1-x)$  mol%  $\text{RuO}_2 + x$  mol%  $\text{SiO}_2$ . This was confirmed using a large amount of experimental data[13, 16-18, 28, 29]. Moreover, as shown in Fig. 3, the equilibrium energies of the  $\text{Ru}_{1-x}\text{Si}_x\text{O}_2$  supercells exhibit a non-monotonic change, by increasing initially and then decreasing, which suggests an interaction between  $\text{RuO}_2$  and  $\text{SiO}_2$ . By polynomial fitting, the relationship between  $E_0$  and the Si doping amount  $x$  can be obtained, as shown in Equation (2).

$$E = -7.4275 + 0.31374x - 0.89392x^2 + 0.28487x^3 \quad (2)$$

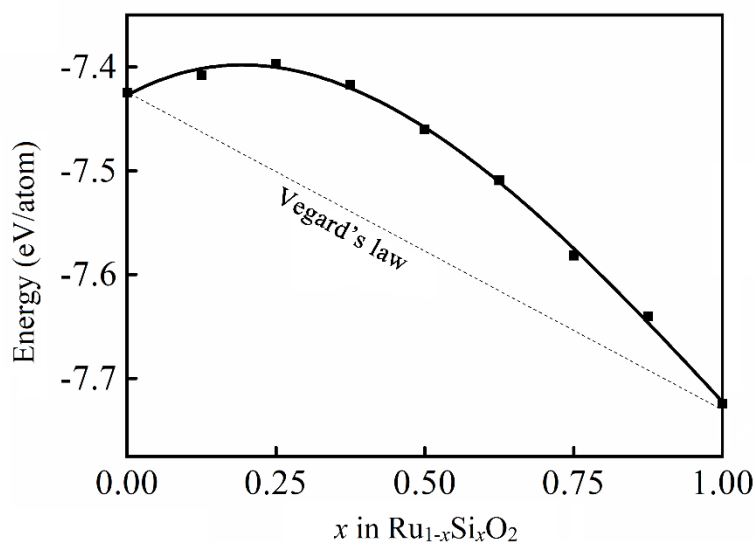


**Figure 3.** Calculated total energies of  $\text{Ru}_{1-x}\text{Si}_x\text{O}_2$  as a function of doping concentration.

### 3.2 Lattice Parameters of Rutile $\text{Ru}_{1-x}\text{Si}_x\text{O}_2$

Based on the Murnaghan equation fitting results, we determined the equilibrium state volume  $V_0$  of each  $\text{Ru}_{1-x}\text{Si}_x\text{O}_2$  supercell and calculated the lattice parameters ( $a$  and  $c$ ) for different Si concentrations ( $x$ ). For the specific calculation process, please refer to the relevant report. The lattice parameter results were found to be in very good agreement with other reported results. For example, the difference between the unit cell parameters of rutile  $\text{RuO}_2$  ( $a = 4.50273 \text{ \AA}$ ,  $c = 3.12546 \text{ \AA}$ ) and the standard JCPDS data ( $a = 4.4994 \text{ \AA}$ ,  $c = 3.1071 \text{ \AA}$ ) is less than 0.6%, and that of rutile  $\text{SiO}_2$  lattice parameters ( $a = 4.23525 \text{ \AA}$ ,  $c = 2.69122 \text{ \AA}$ ) and reported values[30] is less than 2%. According to the calculation results, the fitting formula of rutile  $\text{Ru}_{1-x}\text{Si}_x\text{O}_2$  lattice parameters can be obtained via polynomial fitting, as follows:

$$a(\text{\AA}) = 4.50273 + 0.23858x - 0.16091x^2 - 0.33865x^3 \quad (3)$$

$$c(\text{\AA}) = 3.12546 - 0.98375x - 0.23620x^2 - 0.30330x^3 \quad (4)$$

As illustrated in Fig. 4a, the lattice parameters of  $\text{Ru}_{1-x}\text{Si}_x\text{O}_2$  significantly deviate from Vegard's law with a change in  $x$ , which differs in the  $\text{RuO}_2\text{-SnO}_2$  and  $\text{RuO}_2\text{-ZrO}_2$  systems. It is noteworthy that with an increase in  $x$ , two lattice parameters show opposite non-monotonic changes: parameter  $a$  increases first and then decreases, whereas  $c$  decreases first and then increases. In particular, we

calculated the  $c/a$  ratio, and as shown in Fig. 4b, the curve shows a decreasing trend followed by an increase. The  $c/a$  ratio of rutile  $\text{RuO}_2$  is 0.694, and when  $\text{SiO}_2$  is doped to about 58 mol%, the  $c/a$  ratio drops to a minimum value of 0.597, which is -14.0% of that of the original  $\text{RuO}_2$ , and finally rises to 0.635, which is similar to that of rutile  $\text{SiO}_2$ . Obviously, with an increase in the substitution of  $\text{Si}^{4+}$  for  $\text{Ru}^{4+}$ , the squareness of the rutile lattice fluctuates significantly, which implies that the crystal lattice undergoes varying degrees of distortion, further indicating that there is a strong interaction between  $\text{RuO}_2$  and  $\text{SiO}_2$ .

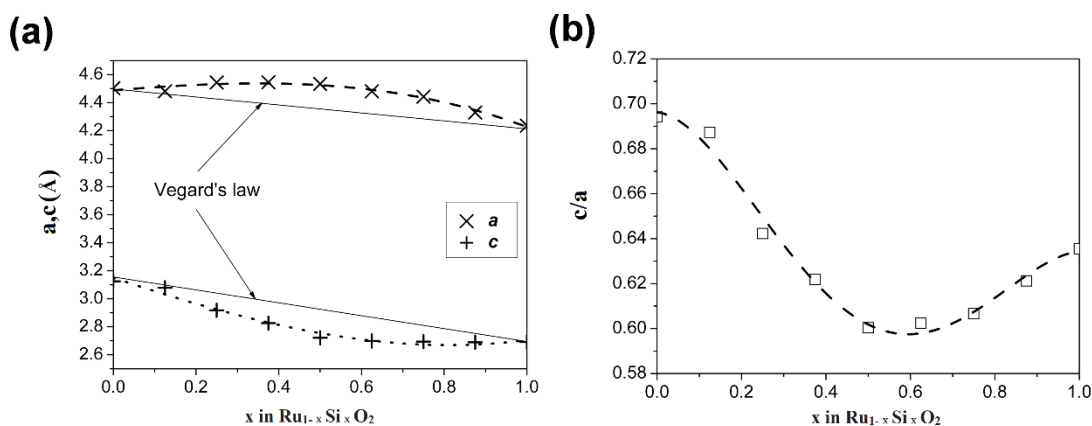


**Figure 4.** Relation curve for doping concentration  $x$  and rutile  $\text{Ru}_{1-x}\text{Si}_x\text{O}_2$  lattice parameters (a)  $a$ ,  $c$ , and (b)  $c/a$ .

### 3.3 Phase Structure of $\text{Ru}_{0.5}\text{Si}_{0.5}\text{O}_2/\text{Ti}$ Electrode Annealed at Different Temperatures

Fig. 5 shows the XRD patterns of the  $\text{Ru}_{0.5}\text{Si}_{0.5}\text{O}_2/\text{Ti}$  electrodes prepared at different annealing temperatures and the diffraction peaks fitted with a Gaussian function. There is a diffraction peak of the titanium substrate for each sample (Fig. 5a). No diffraction peaks other than those for Ti were observed for the samples annealed at 240 °C using thermal decomposition, but a broad diffraction peak curve appeared at  $2\theta = \sim 23\text{--}31^\circ$  (Fig. 5b), which is typical for amorphous structure coating. The XRD patterns of the samples annealed at 260 and 280 °C showed characteristic peaks of the rutile phase. This is an annealing treatment slightly above the crystallization temperature, producing a tiny rutile phase in the amorphous structure. Although the intensity of the rutile phase pattern is not high, characteristic diffraction peaks can still be located with the Ti peak as internal standard, and they were found to deviate from the diffraction peak of pure  $\text{RuO}_2$ , as shown in Figs. 5c and 5d. As predicted, the rutile phase obtained by thermal decomposition followed by a treatment at slightly higher than the crystallization temperature retains a state of high Si doping.

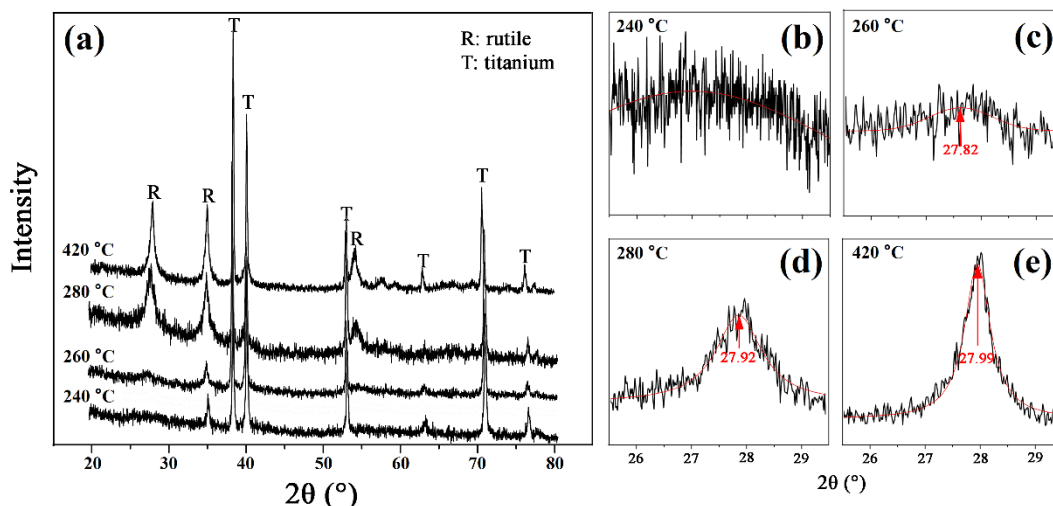


**Figure 5.** (a) XRD patterns of  $\text{Ru}_{0.5}\text{Si}_{0.5}\text{O}_2/\text{Ti}$  electrodes and diffraction peak of samples annealed at (b) 240 °C, (c) 260 °C, (d) 280 °C, and (e) 420 °C.

To calibrate the Si doping concentration of the prepared  $\text{Ru}_{0.5}\text{Si}_{0.5}\text{O}_2$  rutile phase, we attempted to correct the obtained lattice parameters using pure  $\text{RuO}_2$  card data as a standard. After the polynomial fitting, the formula for the influence of the lattice parameters on the Si concentration was obtained, as shown in Equations (5) and (6).

$$a(\text{\AA}) = 4.49940 + 0.39198x - 0.83866x^2 + 0.16834x^3 \quad (5)$$

$$c(\text{\AA}) = 3.10710 - 1.54780x + 2.17126x^2 - 1.13791x^3 \quad (6)$$

Therefore, using Equations (5) and (6), the rutile phases of the samples annealed at 260 and 280 °C were estimated to have Si doping concentrations of about 21.0 and 8.1 mol%, respectively. The characteristic diffraction peak of the conventional crystalline rutile phase appeared for the sample annealed at 420 °C, and its peak position was very close to the pure  $\text{RuO}_2$  card data (Fig. 5e). It was estimated that the doping amount of Si in the rutile phase was only about 2 mol%. This result is consistent with that in the literature[17, 19, 28], indicating that it is difficult to dope the rutile phase at conventional annealing temperatures.

### 3.4 HRTEM Images of $\text{Ru}_{0.5}\text{Si}_{0.5}\text{O}_2$ Coatings Annealed at Different Temperatures

Fig. 6 shows HRTEM images of  $\text{Ru}_{0.5}\text{Si}_{0.5}\text{O}_2/\text{Ti}$  electrodes annealed at different temperatures. As shown in Fig. 6a, the coating annealed at 240 °C has a single-phase structure composed of amorphous crystals, which is consistent with the XRD results. As shown in Fig. 6b, the coating annealed at 260 °C consists of amorphous and microcrystalline crystals with an average grain size of 2-4 nm. Energy Dispersive X-ray (EDX) analysis of the composition of the larger-sized particles showed that the Si content was about 24%, which confirmed that high Si content was indeed present in the crystallites in the early stage of amorphous crystallization. Fig. 6c shows that the coating annealed at 280 °C is composed of amorphous and nanocrystalline crystals, and the average size of the nanocrystals is 4-7 nm. EDX analysis showed that the Si content was about 6%, and that the Si content in the nanocrystals

decreased rapidly. Fig. 6d shows that the rutile crystals in the coating annealed at 420 °C are well-developed, and EDX analysis indicated that the Si content is not high. It was further confirmed that the conventional-temperature (above 400 °C) treatment could only yield nearly pure RuO<sub>2</sub>, which is consistent with the results of previous studies.

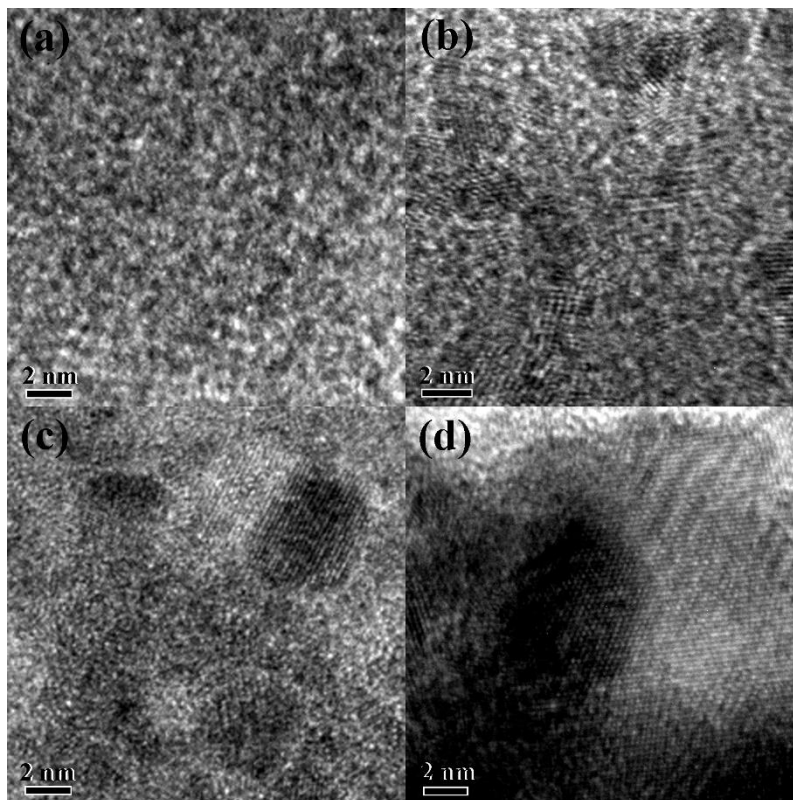
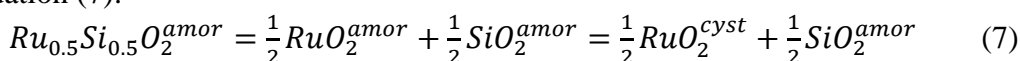


**Figure 6.** HRTEM images of Ru<sub>0.5</sub>Si<sub>0.5</sub>O<sub>2</sub>/Ti electrodes annealed at (a) 240 °C, (b) 260 °C, (c) 280 °C, and (d) 420 °C.

According to the results of XRD and HRTEM, the substitutional doping of Si in the rutile phase can be achieved by thermal decomposition at near-crystallization temperature with an Si/Ru ratio of 1/1. However, as the annealing temperature increases, a lower amount of Si is doped, and if the conventional annealing temperature is applied, it is difficult to dope Si into the rutile phase. This phenomenon is consistent with the recent observation of the phase transition of the binary RuO<sub>2</sub>-MeO<sub>2</sub> system spinodal decomposition[31, 32]. Fig. 3 shows that the equilibrium energy of the Ru<sub>0.5</sub>Si<sub>0.5</sub>O<sub>2</sub> solid solution is about 1.1 eV/mol higher than that of the Ru<sub>0.5</sub>Si<sub>0.5</sub>O<sub>2</sub> composite, which should be the main driving force for the spinodal phase separation. Regarding the spinodal phase separation of Ru<sub>0.5</sub>Si<sub>0.5</sub>O<sub>2</sub>, it can be considered that the precipitation of the rutile phase in the Ru<sub>0.5</sub>Si<sub>0.5</sub>O<sub>2</sub> coating is a result of a combination of decomposition and crystallization of the amorphous phase Ru<sub>0.5</sub>Si<sub>0.5</sub>O<sub>2</sub><sup>amor</sup>, as expressed by Equation (7):



When the amorphous phase is not crystallized (as in the 240 °C sample), Ru<sub>0.5</sub>Si<sub>0.5</sub>O<sub>2</sub><sup>amor</sup> in the coating basically maintains the chemical composition of the precursor, and the Si doping amount of the amorphous phase in the coating is 50 mol%. After heat treatment at near-crystallization temperature (as

for the 260 °C sample),  $\text{Ru}_{0.5}\text{Si}_{0.5}\text{O}_2^{\text{amor}}$  begins to decompose into  $\text{RuO}_2^{\text{amor}} + \text{SiO}_2^{\text{amor}}$ , crystallization occurs in the Ru-rich local region, and rutile crystallites are precipitated. The Si in the crystallites does not diffuse immediately, and hence, a high Si content is retained. With an increase in the annealing temperature, the decomposition and diffusion are more complete, the Si content in the rutile phase decreases, and  $\text{RuO}_2$  is closer to steady state. Furthermore, for another product A that decomposed, with an increase in the annealing temperature, the Ru content decreased, and the amorphous  $\text{SiO}_2$  became more stable. This explains why the rutile phase in the 420 °C sample is close to pure  $\text{RuO}_2$ , which is a good illustration of the root cause of the nearly pure  $\text{RuO}_2$  prepared by conventional-temperature treatment reported in the literature[17, 19, 28].

### 3.5 Electronic Structures of $\text{Ru}_{1-x}\text{Si}_x\text{O}_2$

To investigate the electronic structures of  $\text{Ru}_{1-x}\text{Si}_x\text{O}_2$ , we calculated the band structures as shown in Fig. 7.

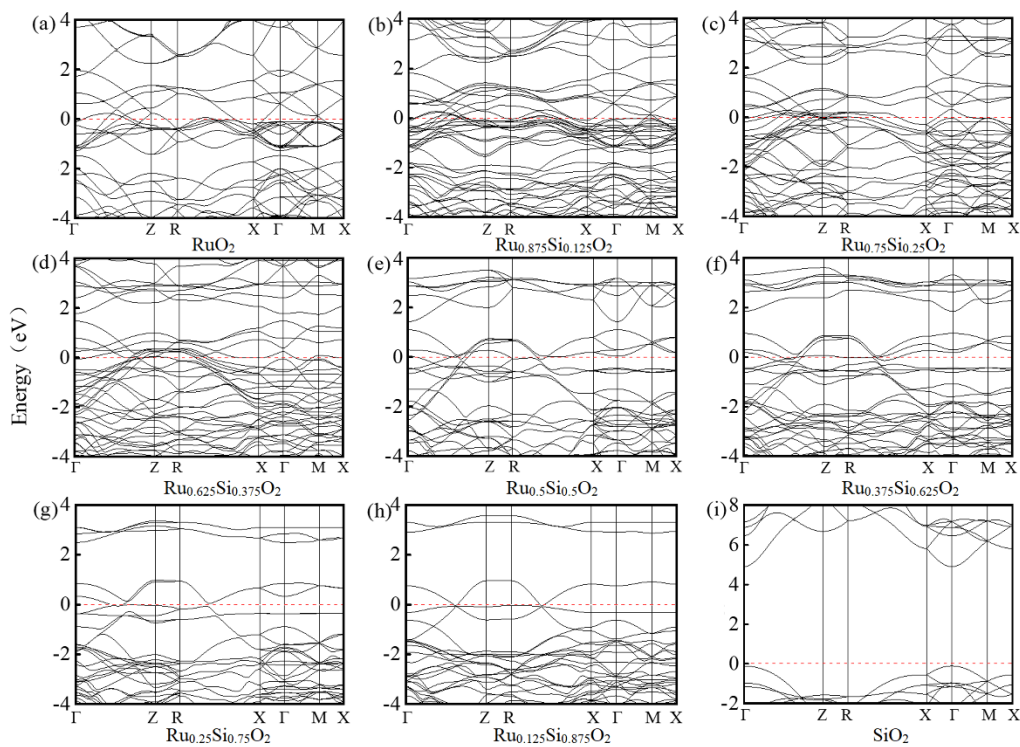


**Figure 7.** Band structures of (a)  $\text{RuO}_2$ , (b)  $\text{Ru}_{0.875}\text{Si}_{0.125}\text{O}_2$ , (c)  $\text{Ru}_{0.75}\text{Si}_{0.25}\text{O}_2$ , (d)  $\text{Ru}_{0.625}\text{Si}_{0.375}\text{O}_2$ , (e)  $\text{Ru}_{0.5}\text{Si}_{0.5}\text{O}_2$ , (f)  $\text{Ru}_{0.375}\text{Si}_{0.625}\text{O}_2$ , (g)  $\text{Ru}_{0.25}\text{Si}_{0.75}\text{O}_2$ , (h)  $\text{Ru}_{0.125}\text{Si}_{0.875}\text{O}_2$ , and (i)  $\text{SiO}_2$ .

The rutile  $\text{RuO}_2$  band (Fig. 7a) suggests a metallic character, which is basically consistent with an earlier report[33], whereas rutile  $\text{SiO}_2$  (Fig. 7i) is a typical insulator with a wide band gap of 5.0 eV, which is in agreement with the results of an earlier study[34]. Fig. 4b-h show that as the Si doping increases, the number of bands near the Fermi level gradually decreases. However, even when the  $x$  is 87.5 mol% (Fig. 7h), the band still passes through the Fermi level, which indicates that  $\text{Ru}_{0.125}\text{Si}_{0.875}\text{O}_2$  still maintains a metallic character. Metallicity is a prerequisite for superior electrode materials, and our

results show that Si can be a large-proportion doping element of a high-quality electrode material. However, the results of some studies[17, 19] do not support this claim. For instance, our team's research[17] indicates that to obtain a material with high activity for chlorine evolution, the Si doping should not exceed 10 mol%. To explain this contradiction, the phase structures must be considered, both for a solid solution and mixture. If a conventional annealing treatment such as the 420 °C annealing described above is employed, the electrode coating is mainly composed of pure  $\text{RuO}_2$  and  $\text{SiO}_2$ ; however, pure  $\text{SiO}_2$  is a harmful component, since it is a typical insulator. The existence of a large amount of insulating  $\text{SiO}_2$  inevitably reduces the conductivity.

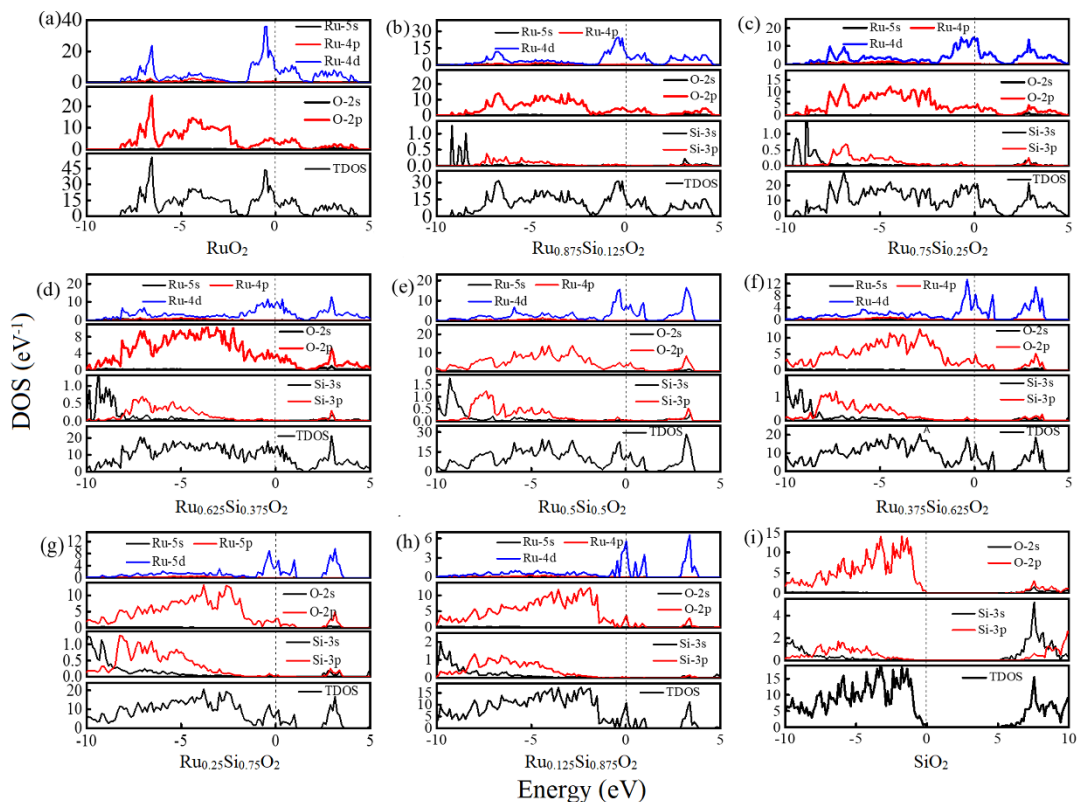


**Figure 8.** Density of states of (a)  $\text{RuO}_2$ , (b)  $\text{Ru}_{0.875}\text{Si}_{0.125}\text{O}_2$ , (c)  $\text{Ru}_{0.75}\text{Si}_{0.25}\text{O}_2$ , (d)  $\text{Ru}_{0.625}\text{Si}_{0.375}\text{O}_2$ , (e)  $\text{Ru}_{0.5}\text{Si}_{0.5}\text{O}_2$ , (f)  $\text{Ru}_{0.375}\text{Si}_{0.625}\text{O}_2$ , (g)  $\text{Ru}_{0.25}\text{Si}_{0.75}\text{O}_2$ , (h)  $\text{Ru}_{0.125}\text{Si}_{0.875}\text{O}_2$ , and (i)  $\text{SiO}_2$ .

The density of states (DOS) was calculated as shown in Fig. 8. For  $\text{RuO}_2$  (Fig. 8a), the valence band occupied at the Fermi level, indicating a metallic character, and the conduction band are mainly contributed by Ru-4d electrons and a few O-2p electrons, which is consistent with an earlier report. As shown by the total DOS (TDOS), with an increase in Si-doping concentration (Fig. 8b-h), the valence band maximum gradually moves down, whereas the conduction band minimum shifts up, and the peak in the low-energy area of the conduction band gradually becomes shorter and narrower, suggesting an attenuating conductivity. The partial DOS (PDOS) indicates that although Si-3p electrons contribute in varying degrees to the conduction band, the primary conductive suppliers are still Ru-4d and O-2p electrons, which explains the attenuating conductivity with Si-doping, as indicated by the TDOS.

### 3.6 Conductivity of Ru<sub>1-x</sub>Si<sub>x</sub>O<sub>2</sub>

According to the theory of semiconductor physics, the conductivity can be expressed using the formula:

$$\delta = nq\mu \quad (8)$$

where  $n$  is the carrier concentration, the electric quantity  $q$  is a constant,  $\mu$  is the electron mobility, and

$$\mu \propto \frac{q}{m^*N} \quad (9)$$

where  $m^*$  is the effective mass of electrons,  $N$  is the doping concentration. Therefore, for the different compositions of Si-doped Ru<sub>1-x</sub>Si<sub>x</sub>O<sub>2</sub>, the conductivity ratio  $\delta_x/\delta_y$  can be represented as follows:

$$\frac{\delta_x}{\delta_y} = \frac{n_x m_y^* N_y}{n_y m_x^* N_x} \quad (10)$$

wherein  $n$  can be calculated using the integral method according to the position of the Fermi level in the conduction band, and  $m^*$  can be calculated from the lowest energy level of the conduction band, using the derivative  $\left(\frac{d^2E}{dk^2}\right)^{-1}$ . Thus, the ratio  $\delta_x/\delta_0$  can be applied to exhibit the change in conductivity with an increase in the doping concentration, and we also calculated  $\delta_x/\delta_{0.125}$  and  $\delta_x/\delta_{0.25}$  for comparison. As shown in Fig. 9, the concentration of Si-doping has a great influence on the conductivity ratio  $\delta_x/\delta_0$ , with a tendency for exponential attenuation. The conductivity fitting formula was obtained as follows:

$$\frac{\delta_x}{\delta_0} = 1.092 \cdot \exp\left(-\frac{x}{0.231}\right) \quad (11)$$

When the correlation coefficient is 0.999, according to the fitting formula, the effect of Si-doping on the conductivity of rutile RuO<sub>2</sub> is theoretically consistent with the first-order exponential attenuation relationship.

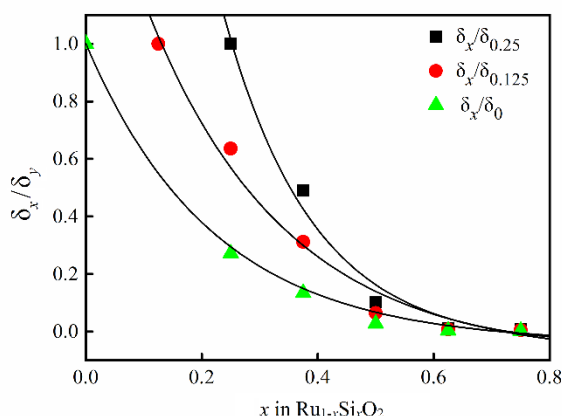


**Figure 9.** Conductivity ratio  $\delta_x/\delta_y$  as a function of doping concentration  $x$ .

### 3.7 Conductivity of Ru<sub>0.5</sub>Si<sub>0.5</sub>O<sub>2</sub>/Ti Electrodes Annealed at Different Temperatures

In this study, samples of Ru<sub>0.5</sub>Si<sub>0.5</sub>O<sub>2</sub> annealed at different temperatures were tested using the AC impedance method. The test data was processed using the ZSimpWin software. Fig. 10 show the Bode

plots and Bode phase diagrams of Ru<sub>0.5</sub>Si<sub>0.5</sub>O<sub>2</sub>/Ti electrodes annealed at different temperatures, respectively.

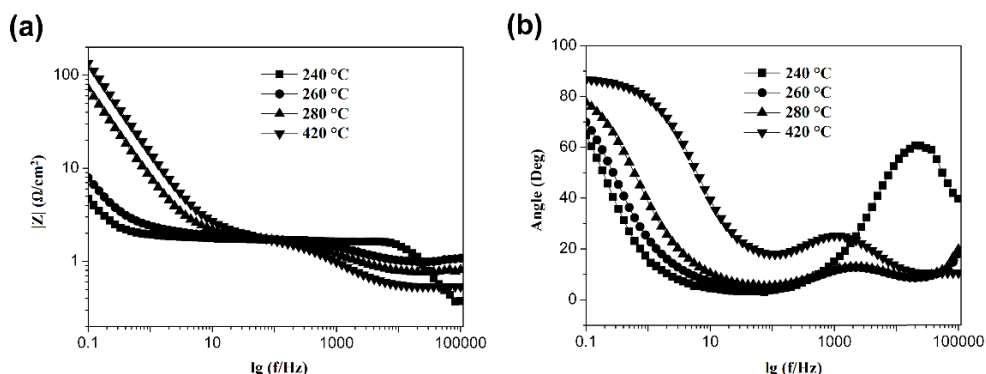


**Figure 10.** (a) Bode plots and (b) Bode phase diagrams of Ru<sub>0.5</sub>Si<sub>0.5</sub>O<sub>2</sub>/Ti electrodes.

The  $|Z|-\lg f$  and  $\Phi-\lg f$  curves of the sample, similar to those reported in the literature[35, 36], can be fitted with an equivalent electrical circuit (EEC) containing two time-constants. For the samples annealed from 260 to 420 °C, the  $R_s(R_1Q_1)(R_2Q_2)$  method is used to fit the data.  $R_s$  is the solution resistance,  $(R_1Q_1)$  is the impedance of the high-frequency band, and  $(R_2Q_2)$  is the impedance of the low-frequency band. For samples annealed at 240 °C, the Warburg impedance in the low-frequency band can be increased, and the corresponding EEC can be expressed as  $R_s(R_1Q_1)((R_2W)Q_2)$ . Fig. 10 shows that the total impedance  $|Z|$  of each sample shows a gradual decrease with an increase in the AC frequency; the phase angle  $\Phi$  shows two peaks with an increase in the AC frequency. This is very similar to the results of the Ru-Ti oxide mentioned in the literature[37]. Different annealing temperatures have a significant effect on sample impedance and phase angle. In particular, as the annealing temperature increases, the phase separation of the sample increases and the impedance of the sample rises rapidly.

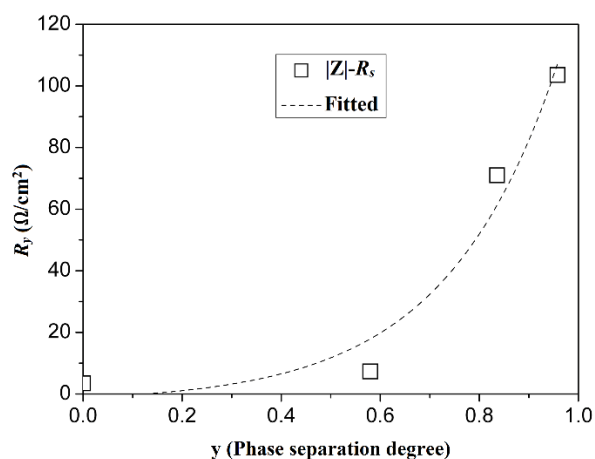


**Figure 11.** Resistance as a function of phase separation degree.

For a sample of  $\text{Ru}_{0.5}\text{Si}_{0.5}\text{O}_2$  with Si in the rutile phase,  $y$  ( $y = (0.5 - x)/0.5$ ) is used to indicate the degree of phase separation, along with  $R_y$  ( $R_y = |Z| - R_s$ ). This indicates the coating resistance of the sample; using the conductivity  $\delta_y = d/R_y$  ( $d$  is the thickness of the coating), the relationship between the resistance of the sample and the degree of phase separation can be derived (see Fig. 11). The sample resistance  $R_y$  is in an exponential growth relationship with the degree of phase separation, as shown in Equation (12).

$$R_y = 1.583 \cdot \exp\left(\frac{y}{0.2259}\right) - 2.766 \quad (12)$$

For a certain composition of the  $\text{Ru}_{1-x}\text{Si}_x\text{O}_2$  electrode, the degree of phase separation also has an exponential effect on its electrical conductivity. To describe the conductivity attenuation of the phase-separated  $\text{Ru}_{1-x}\text{Si}_x\text{O}_2$  electrode, choosing pure  $\text{RuO}_2$  as the reference, the ratio  $\delta'_y/\delta_0 = \delta'_y/\delta_x \cdot \delta_x/\delta_0 = \delta'_y/\delta'_0 \cdot \delta_x/\delta_0$  can be used; this includes two factors: the phase separation factor  $\delta'_y/\delta'_0$  and Si doping factor  $\delta_x/\delta_0$ . For the 420 °C annealed  $\text{Ru}_{0.5}\text{Si}_{0.5}\text{O}_2$  sample,  $\delta'_y/\delta'_0 = \delta'_{0.958}/\delta'_0 = R_0/R_{0.958} = 0.033$ ,  $\delta_x/\delta_0 = \delta_{0.5}/\delta_0 = 0.065$ ; therefore, the conductivity attenuation is  $\delta'_{0.958}/\delta_0 = 0.0022$ . In addition, we collected data from related literature[28] and found that the conductivity is also in accordance with exponential attenuation: with an increase in the Si-doping concentration, the attenuation rate is higher. According to the reported data of a 400 °C annealed sample with approximately 100% phase separation, we extrapolated the conductivity ratio of  $\text{Ru}_{0.5}\text{Si}_{0.5}\text{O}_2$  to  $\delta'_y/\delta'_0 = 0.0025$ , which is very close to our result of 0.0022 for the 420 °C annealed sample. It is obvious that the conductivity decay rate of the actual electrode material is very fast, which can be attributed to the combination of the Si doping attenuation and the phase separation attenuation.

In consideration of the fact that  $\text{RuO}_2\text{-SiO}_2$  is an easily decomposable system, it is necessary to take into account the influence of phase separation. If conventional annealing is used, the material is composed of pure  $\text{RuO}_2$  and  $\text{SiO}_2$ . Since pure  $\text{SiO}_2$  is a typical insulator, which is harmful to conductive materials or active materials, the existence of phase separation inevitably reduces the conductivity of the materials. Therefore, to obtain high-quality electrode materials, efforts should be made to avoid or hinder the exsolution and decomposition of the Si-doped phase.

#### 4. CONCLUSIONS

In conclusion, combined with experimental characterization methods such as XRD, HRTEM, and impedance analysis, we carried out first-principles calculations to investigate the stability, crystal structure, electronic structure, and conductivity of the  $\text{RuO}_2\text{-SiO}_2$  binary oxide. Our results show that  $\text{Ru}_{1-x}\text{Si}_x\text{O}_2$  solid solutions are unstable owing to higher total energy than that of the composite, and that the total energy and lattice parameters of  $\text{Ru}_{1-x}\text{Si}_x\text{O}_2$  solid solutions significantly deviate from Vegard's law, indicating that there is a strong interaction between  $\text{RuO}_2$  and  $\text{SiO}_2$ , which explains why reported Si-containing materials are mostly  $\text{RuO}_2\text{+SiO}_2$  composites but not solid solutions. The Si-doped  $\text{RuO}_2$  prepared using thermal decomposition at different annealing temperatures show varying degrees of phase separation, and the phase analysis of  $\text{Ru}_{0.5}\text{Si}_{0.5}\text{O}_2$  confirmed that substitutional doping of Si in the rutile phase can be achieved by near-crystallization-temperature annealing. The band structures suggest that  $\text{Ru}_{1-x}\text{Si}_x\text{O}_2$  still maintains a metallic state even when the Si doping concentration is 87.5 mol%,

which provides a theoretical basis for high Si doping. The density of states shows that the primary conductive contributors are Ru-4d and O-2p electrons, and further calculations indicate that the conductivity of  $\text{Ru}_{1-x}\text{Si}_x\text{O}_2$  attenuates with a first-order exponent with an increase in Si doping concentration. Furthermore, the EIS test results show that the impedance of  $\text{Ru}_{1-x}\text{Si}_x\text{O}_2$  and the degree of phase separation are also consistent with the first-order exponential relation. Based on this study, it is practical to achieve high-quality Si-doped  $\text{RuO}_2$  as electrode materials; controlling the doping concentration and avoiding phase separation are key factors in maintaining high conductivity.

#### ACKNOWLEDGMENTS

We gratefully acknowledge the financial support from Natural Science Foundation of China (11374053, 11104031, 51171046 and 21875038), National High Technology Research and Development Projects (863) of China (2007AA03Z325), the central financial aid for innovation team building (2012-FD-02), Science and Technology Project of Fujian Provincial Education Department (JK2017005) and Natural Science Foundation of Fujian Province (2013J01175).

#### References

1. Z.J. Chen, J.Q. Zhu, S. Zhang, Y.Q. Shao, D.Y. Lin, J.F. Zhou, Y.X. Chen and D. Tang, *Journal Of Hazardous Materials*, 333 (2017) 232.
2. D.P. Debecker, B. Farin, E.M. Gaigneaux, C. Sanchez and C. Sasso, *Applied Catalysis A:General*, 481 (2014) 11.
3. J. Ma, Y. Wu, J. Zuo, C. Jiang, D.F. Khan, H. Zhang and J. Zhu, *Journal Of Electroanalytical Chemistry*, 789 (2017) 133.
4. Y.N. He, J.Q. Zhu, T. Zhang, X. Wang and D. Tang, *Chinese Journal Of Structural Chemistry*, 32 (2013) 231.
5. S.M.A. Shibli and M.A. Sha, *Journal Of Alloys And Compounds*, 749 (2018) 250.
6. T. Zhang, D. Tang, Y. Shao, X. Ke and S. You, *Journal Of the American Ceramic Society*, 90 (2007) 989.
7. L. Manjakkal, K. Zaraska, K. Cvejic, J. Kulawik, and D. Szwagierczak, *Talanta*, 147 (2016) 233.
8. J.C. Chou, Y.L. Chen, M.H. Yang, Y.Z. Chen, C.C. Lai, H.T. Chiu, C.Y. Lee, Y.L. Chueh and J.Y. Gan, *Journal Of Materials Chemistry A*, 1 (2013) 8753.
9. D.T. Araujo, M.d.A. Gomes, R.S. Silva, C.C. de Almeida, C.A. Martinez-Huitle, K.I.B. Eguiluz, and G.R. Salazar-Banda, *Journal Of Applied Electrochemistry*, 47 (2017) 547.
10. B. Liu, C. Wang and Y. Chen, *Electrochimica Acta*, 264 (2018) 350.
11. P.A. DeSario, C.N. Chervin, E.S. Nelson, M.B. Sassin and D.R. Rolison, *Acs Applied Materials & Interfaces*, 9 (2017) 2387.
12. V. Prabhakaran, G. Wang, J. Parrondo and V. Ramani, *Journal Of the Electrochemical Society*, 163 (2016) F1611.
13. X. Paquez, G. Amiard, G. de Combarieu, C. Boissiere and D. Grosso, *Chemistry Of Materials*, 27 (2015) 2711.
14. L. Zheng, Q. Zeng, S. Liao and J. Zeng, *International Journal Of Hydrogen Energy*, 37 (2012) 13103.
15. A. Kumar and V.K. Ramani, *Applied Catalysis B-Environmental*, 138 (2013) 43.
16. C.P. Lo and V. Ramani, *Acs Applied Materials & Interfaces*, 4 (2012) 6109.
17. X.H. Liu and D. Tang, *Journal of Materials Protection*, 40 (2007) 7.
18. E.V. Jelenkovic, K.Y. Tong, W.Y. Cheung and S.P. Wong, *Microelectronic Engineering*, 71 (2004) 237.

19. V. Parvulescu, V.I. Parvulescu, G. Popescu, A. Julbe, C. Guizard and L. Cot, *Catalysis Today*, 25 (1995) 385.
20. J. Hafner, *Journal Of Computational Chemistry*, 29 (2008) 2044.
21. G. Kresse and J. Furthmuller, *Computational Materials Science*, 6 (1996) 15.
22. G. Kresse and J. Furthmuller, *Physical Review B*, 54 (1996) 11169.
23. P.E. Blochl, *Physical Review B*, 50 (1994) 17953.
24. J.P. Perdew, K. Burke and Y. Wang, *Physical Review B*, 54 (1996) 16533.
25. J.P. Perdew and Y. Wang, *Physical Review B*, 45 (1992) 13244.
26. F.D. Murnaghan, *Proceedings of the National Academy of Sciences of the United States of America*, 30 (1944) 244.
27. A.R. Denton and N.W. Ashcroft, *Physical Review A*, 43 (1991) 3161.
28. J.S. Jeng, Y.T. Lin and J.S. Chen, *Thin Solid Films*, 518 (2010) 5416.
29. L. Armelao, D. Barreca and B. Moraru, *Journal Of Non-Crystalline Solids*, 316 (2003) 364.
30. A.A. Tamijani and E. Ebrahimiaqda, *Solid State Sciences*, 67 (2017) 119.
31. X. Wang, Y.Q. Shao, X.H. Liu, D. Tang, B. Wu, Z.Z. Tang, X. Wang and W. Lin, *Journal Of the American Ceramic Society*, 98 (2015) 1915.
32. Y.M. Li, X. Wang, Y.Q. Shao, D. Tang, B. Wu, Z.Z. Tang and W. Lin, *Physical Chemistry Chemical Physics*, 17 (2015) 1156.
33. N. Mehtougui, D. Rached, R. Khenata, H. Rached, M. Rabah and S. Bin-Omran, *Materials Science In Semiconductor Processing*, 15 (2012) 331.
34. T.M. Muscenti, G.V. Gibbs and D.F. Cox, *Surface Science*, 594 (2005) 70.
35. P.P. Sharma and I.I. Suni, *Journal Of the Electrochemical Society*, 158 (2011) H111.
36. B. Borresen, G. Hagen and R. Tunold, *Electrochimica Acta*, 47 (2002) 1819.
37. B.V. Tilak, V.I. Birss, J. Wang, C.P. Chen and S.K. Rangarajan, *Journal Of the Electrochemical Society*, 148 (2001) L10.

© 2021 The Authors. Published by ESG ([www.electrochemsci.org](http://www.electrochemsci.org)). This article is an open access article distributed under the terms and conditions of the Creative Commons Attribution license (<http://creativecommons.org/licenses/by/4.0/>).